



**HAL**  
open science

## Observation of Gravity Waves at the Tropical Tropopause Using Superpressure Balloons

Milena Corcos, Albert Hertzog, Riwal Plougonven, Aurélien Podglajen

► **To cite this version:**

Milena Corcos, Albert Hertzog, Riwal Plougonven, Aurélien Podglajen. Observation of Gravity Waves at the Tropical Tropopause Using Superpressure Balloons. *Journal of Geophysical Research: Atmospheres*, 2021, 126 (15), pp.e2021JD035165. 10.1029/2021JD035165 . hal-03402825

**HAL Id: hal-03402825**

**<https://hal.science/hal-03402825>**

Submitted on 26 Oct 2021

**HAL** is a multi-disciplinary open access archive for the deposit and dissemination of scientific research documents, whether they are published or not. The documents may come from teaching and research institutions in France or abroad, or from public or private research centers.

L'archive ouverte pluridisciplinaire **HAL**, est destinée au dépôt et à la diffusion de documents scientifiques de niveau recherche, publiés ou non, émanant des établissements d'enseignement et de recherche français ou étrangers, des laboratoires publics ou privés.

# 1 Observation of gravity waves at the tropical 2 Tropopause using superpressure balloons

3 Milena Corcos<sup>1</sup>, Albert Hertzog<sup>1</sup>, Riwal Plougonven<sup>2</sup>, Aurélien Podglajen<sup>3</sup>

4 <sup>1</sup>Laboratoire de Météorologie Dynamique/IPSL, Sorbonne Université, Paris, France

5 <sup>2</sup>Laboratoire de Météorologie Dynamique/IPSL, Ecole Polytechnique, Institut Polytechnique de Paris,  
6 France

7 <sup>3</sup>Laboratoire de Météorologie Dynamique/IPSL, CNRS, Ecole Polytechnique, Institut Polytechnique de  
8 Paris, France

## 9 Key Points:

- 10 • Tropical gravity wave activity is characterized from long-duration superpressure  
11 balloon flights.
- 12 • Gravity-wave momentum fluxes exhibit a clear dependence to the distance on the  
13 nearest convective system.
- 14 • Observed wave intermittency results from the time- and spatially-varying distri-  
15 bution of the source.

---

16 Corresponding author: Milena Corcos, [milena.corcos@lmd.ipsl.fr](mailto:milena.corcos@lmd.ipsl.fr)

17 **Abstract**

18 Tropical gravity wave activity is investigated using measurements of momentum fluxes  
 19 gathered during Strateole-2 superpressure balloon flights. The dataset consists of 8 balloon  
 20 flights performed in the deep tropics from November 2019 to February 2020. The flights  
 21 lasted for 2 to 3 months each, and in-situ meteorological data were collected every 30 s.  
 22 The relation between gravity waves and deep convection is investigated using geostationary  
 23 satellite data from the NOAA/NCEP GPM\_MERGIR satellite data product, at 1 hour  
 24 resolution. The amplitude of gravity wave momentum fluxes shows a clear dependence on  
 25 the distance to the nearest convective system, with a strong decay as distance to convection  
 26 increases. The largest momentum-flux values ( $> 5$  mPa) are only found less than 200 km  
 27 away from deep convection. The sensitivity of the wave flux to distance from convection  
 28 is stronger for high frequency gravity waves (periods shorter than 60 minutes). Lower  
 29 frequency waves tend to a non-zero, background value away from convection, supporting  
 30 some background value in gravity-wave drag parameterizations. On the other hand, the wide  
 31 range of momentum flux values observed close to the convection emphasizes the intermittent  
 32 nature of the gravity-wave source. The large scale variation of gravity-wave intermittency  
 33 within the equatorial belt is also studied. The results highlight spatial variations of gravity  
 34 wave activity, with the highest momentum flux recorded over land.

35 **1 Introduction**

36 Tropical deep convection excites a broad range of waves. At the low-frequency end,  
 37 planetary-scale equatorial waves, like Kelvin or Yanai waves, have periods of a few to tens  
 38 of days and horizontal scales that are a fraction of the Earth circumference (Matsuno, 1966).  
 39 At the high-frequency end, gravity waves have periods as low as a few minutes and horizontal  
 40 scales as short as that of individual convective cells. Yet, despite their short temporal and  
 41 spatial scales, gravity waves significantly impact the global tropical atmosphere. They can  
 42 influence synoptic systems (Lane & Moncrieff, 2008; Piani et al., 2000), and are an essential  
 43 driver of the Quasi-Biennial Oscillation (QBO) together with (or even more importantly  
 44 than) planetary waves (Dunkerton & Dunkerton, 1997; Ern et al., 2008; Kawatani et al.,  
 45 2010; Ern et al., 2014). At smaller scales, gravity waves initiate cirrus clouds and modulate  
 46 their life cycle (Podglajen et al., 2016; Dinh et al., 2016; Jensen et al., 2016; Podglajen  
 47 et al., 2018), which both impact the local dynamics and the global climate (Fueglistaler &  
 48 Baker, 2006; Jensen et al., 2010; Solomon et al., 2010). Last, all tropical waves contribute  
 49 to modulating the tropopause temperature, and thus influence water vapor transport to the  
 50 stratosphere (Kim & Alexander, 2015).

51 Whereas the resolution of atmospheric general circulation models enables the explicit res-  
 52 olution of large-scale waves in most circumstances, it remains too coarse to fully resolve  
 53 shorter-scale gravity waves. These are notably parameterized in climate models in order to  
 54 represent their significant contribution in shaping the mean circulation of the middle atmo-  
 55 sphere (Fritts, 1993; Holton et al., 1995; Fritts & Alexander, 2003). In particular, the QBO,  
 56 which is a major feature of the Earth climate (Baldwin et al., 2001), is partly driven by grav-  
 57 ity waves, and its simulation in climate models remains particularly challenging (Schirber  
 58 et al., 2015; Butchart et al., 2018; Holt et al., 2020). The evolution of the QBO under  
 59 climate change is furthermore currently unclear (Richter et al., 2020), calling for enhanced  
 60 observational constraints on tropical gravity waves to improve parameterizations.

61 In the deep tropics, moist convection is the most prominent source of gravity waves: satellite  
 62 observations have for instance shown the coincidence in location and seasonality of strato-  
 63 spheric gravity waves and deep tropospheric convection (Alexander et al., 2008; Ern et  
 64 al., 2011). Mechanisms involved in convective gravity-wave generation have been revealed  
 65 thanks to idealized simulations of numerical models (Alexander et al., 1995; Piani et al.,  
 66 2000; Lane et al., 2001). Convective gravity waves have also been observed with further  
 67 techniques like radar (Larsen et al., 1982), aircrafts (Pfister et al., 1993; Alexander & Pfis-

68 ter, 1995; Jensen et al., 2013), and radiosoundings (Karoly et al., 1996; Dhaka et al., 2011).  
 69 Yet, because of their short spatial scales and of their intermittency, global observations of  
 70 gravity waves remain challenging (Alexander et al., 2010). To better constrain gravity-wave  
 71 parameterizations in global models therefore requires more observations.

72 In the present study, we use observations gathered during long-duration stratospheric  
 73 balloon flights within the Strateole-2 project (Haase et al., 2018). Strateole-2 will release  
 74 a total of 50 long-duration balloons in three campaigns between 2019 and 2024. Those  
 75 balloons are intended to drift around the whole tropical belt to enable studies of climate  
 76 processes in the Tropical Tropopause Layer (TTL) and the lower stratosphere. Since they  
 77 can fly for months, continuous observations at high-resolution performed during the flights  
 78 provide unique measurements on the global activity of gravity waves (Boccaro et al., 2008;  
 79 Vincent et al., 2007; Hertzog et al., 2008; Hertzog & Vial, 2001; Jewtoukoff et al., 2013),  
 80 with a potential to provide valuable insights on their contribution to the QBO (Vincent &  
 81 Alexander, 2020).

82 This study is thus aimed at characterizing equatorial gravity-wave activity during boreal  
 83 winter, and at describing its relation to deep convection. After describing the dataset used  
 84 and our methodology in Section 2, we present in Section 3 a case study of a large gravity-  
 85 wave momentum-flux event, associated with a convective complex in the intertropical con-  
 86 vergence zone (ITCZ). In Section 4, we statistically study the dependence between recorded  
 87 momentum fluxes and the balloon distance to convective cells. The discussion section then  
 88 addresses the observed differences in the behavior of short- and long-period gravity waves,  
 89 as well as geographical contrasts in wave activity and intermittency in the tropics. The last  
 90 section of the article is devoted to a brief summary and conclusion.

## 91 2 Data and Methodology

### 92 2.1 Balloon observations

93 Gravity-wave information used in this study is derived from observations collected by  
 94 superpressure balloons in the deep tropics. These flights were performed during boreal  
 95 winter (November 2019 – February 2020), within the first Strateole-2 campaign. The tra-  
 96 jectory of the 8 balloons released from Seychelles Islands (55.52°E, 4.67°S) during this  
 97 campaign are displayed in Figure 1. To a good approximation, superpressure balloons drift  
 98 on constant-density surfaces in the atmosphere (Hertzog & Vial, 2001), and thus behave  
 99 as quasi-Lagrangian tracers in the flow. During the campaign, two different flight levels  
 100 were used. Low-level “TTL” flights flew at  $\sim 19$  km, typically 1.5 km above the Cold-Point  
 101 Tropopause (CPT), near the top of the TTL. Higher-level “STR” flights on the other hand  
 102 flew at  $\sim 20.5$  km, in the stratosphere. The mean altitude and pressure of each of the flights  
 103 are reported in Table 1. All observations were collected within  $20^\circ$  of the equator.

Every balloon carried a GPS receiver and a Tsen instrument (Thermodynamical sensor),  
 which records the in-situ air pressure and temperature (Hertzog et al., 2004, 2007). Both  
 the GPS receiver and the Tsen provide observations every 30 s during the flights. In theory,  
 this time resolution enables us to resolve the full spectrum of atmospheric waves in the  
 tropical lower stratosphere. As usually performed with superpressure balloon observations,  
 the zonal and meridional components of the wind are deduced from successive positions  
 of the balloon, with a precision of  $\sim 0.1$  m/s (Vial et al., 2001; Podglajen et al., 2014).  
 The air-parcel vertical displacements ( $\zeta'$ ), on the other hand, are inferred from the pressure  
 timeseries: the pressure measurements are preferred over the raw GPS records, since they  
 have a higher precision (0.1 hPa, typically corresponding to 0.1 m at the balloon flight level)  
 than the GPS altitudes (precision of  $\sim 1.5$  m). ~~Assuming hydrostaticity and a perfect~~  
~~isopycnic behavior of the balloon~~ (Podglajen et al., 2016). Actually, the wave-induced total

Table 1: Characteristics of 2019 Strateole-2 balloon flights

Flight	Altitude (km)	Pressure (hPa)	Launch (UT)	End (UT)	Duration (day)
01_STR1	20.7	50.8	2019-11-12	2020-02-28	107
02_STR2	20.2	55.0	2019-11-11	2020-02-23	103
03_TTL3	19.0	66.2	2019-11-18	2020-02-28	101
04_TTL1	18.8	69.4	2019-11-27	2020-02-02	66
05_TTL2	18.9	67.6	2019-12-05	2020-02-23	79
06_STR1	20.5	51.4	2019-12-06	2020-02-01	57
07_STR2	20.2	54.8	2019-12-06	2020-02-28	83
08_STR2	20.2	54.6	2019-12-07	2020-02-22	77

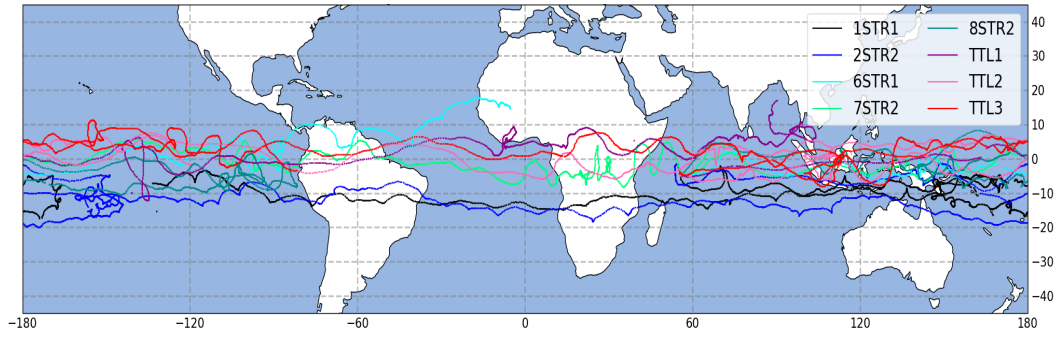


Figure 1: Map of the eight superpressure balloon flights of the first Strateole-2 campaign, which were launched in November-December 2019.

pressure disturbances ( $p'_T$ ) measured by superpressure balloons read:

$$p'_T = p' + \frac{d\bar{p}}{dz} \zeta'_b \quad (1)$$

where the first term in the RHS corresponds to the Eulerian pressure perturbations ( $p'$ ), and the second term is a Lagrangian contribution associated with the vertical displacement of the balloon ( $\zeta'_b$ ) in the background pressure gradient ( $\frac{d\bar{p}}{dz}$ ). For wave motions with intrinsic periods longer than  $2\tau_N$ , where  $\tau_N = 2\pi/N \sim 4.5$  min is the Brunt-Väisälä period in the tropical lower stratosphere, superpressure balloons stay on constant-density surfaces (Vincent & Hertzog, 2014). Their vertical displacements are then readily related to those of air parcels:

$$\zeta' = \frac{g/c_p + d\bar{T}/dz}{g/R + d\bar{T}/dz} \zeta'_b \quad (2)$$

where  $g$  is the gravitational acceleration,  $c_p$  and  $R$  are the heat capacity at constant pressure and the perfect gas constant per unit mass respectively, and  $d\bar{T}/dz$  the background vertical gradient of temperature.

The balloon timeseries, i.e. 3D wind, temperature and vertical displacement, are then processed through a wavelet analysis, as was done in Hertzog and Vial (2001), Boccara et al. (2008) and Hertzog et al. (2012). The wavelet analysis provides information in the time/intrinsic-frequency domain for each of the timeseries. We use a complex Morlet mother wavelet, which enables us to retrieve the local amplitude and phase of the signals every 30 s on a finite number of intrinsic frequencies ( $\hat{\omega}_i$ ) (Torrence & Compo, 1998). Gravity-wave momentum fluxes are inferred from the cross-correlation of total-pressure and horizontal-wind disturbances. Here, we take benefit from the fact that the two terms in the RHS of Equation (1) are in phase quadrature, so that only the cross-correlation with the second term (that is linked to the air-parcel vertical displacements) is retained (see, e.g., Equation (26) in Vincent and Hertzog (2014)). The wavelet coefficients are then combined and summed over the intrinsic frequency axis to obtain timeseries of e.g. temperature variances  $\overline{T'^2(t)}$  or zonal momentum fluxes  $\overline{\bar{\rho} u' w'(t)}$ , where  $\bar{\rho}$  is the flight-averaged balloon density. The gravity-wave polarization relations are also used to infer the local wave direction of propagation (Fritts & Alexander, 2003), and thus the total momentum-flux timeseries  $\overline{\bar{\rho} u'_{\parallel} w'(t)}$ , which is the sum of the absolute momentum fluxes over all propagation directions.

Note that temperature fluctuations ( $T'$ ) used in this study were also reconstructed from the air-parcel vertical displacements according to the adiabatic equation:

$$T' = -\frac{g}{c_p} \zeta', \quad (3)$$

which typically holds for periods shorter than a few days in the tropical lower stratosphere. Temperature disturbances obtained this way are generally less noisy than the raw temperature measurements: since superpressure balloons move with the wind, the ventilation of temperature sensors on such flights is very weak, and the measured temperature may deviate from that of the air, especially during daytime (Hertzog et al., 2004). In Equation (3), the air-parcel vertical displacement is inferred from Equations (1) and (2), where we have assumed that the Eulerian pressure perturbations are negligible compared to the Lagrangian ones. This assumption is notably valid for low-frequency waves, which are those that contribute the most to the temperature variances (see discussion at the end of this section).

When a superpressure balloon flies over a deep convective system at night, the associated decrease of outgoing infrared flux may cause the balloon to depressurize. In such circumstances, the balloon volume decreases, and the balloon temporarily lowers its flight level by a few hundred meters typically until the longwave flux increases back or the sun rises. During a depressurization event, the balloon behavior is therefore no longer isopycnic. Wavelet coefficients influenced by such events were discarded from the following analysis. Those events represent less than 5% of the data from all the flights.

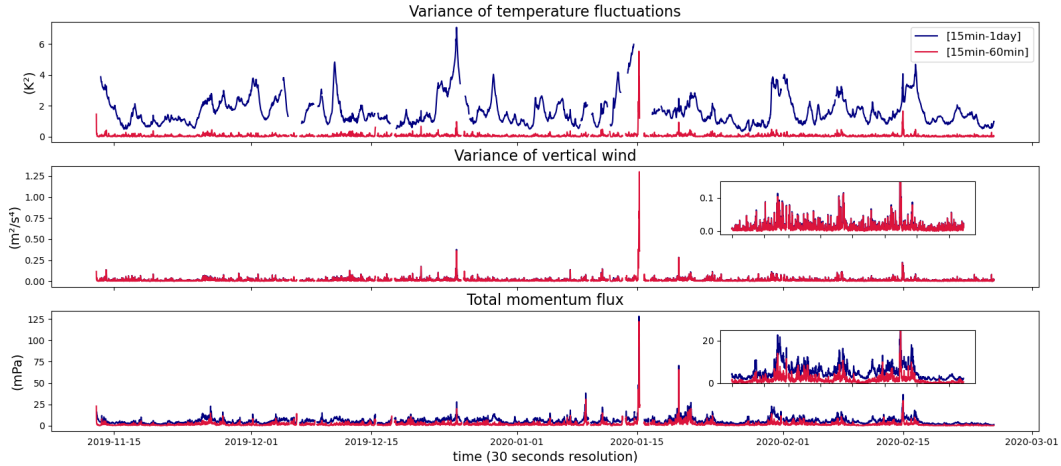


Figure 2: Timeseries of variance of temperature (top panel), vertical wind (middle panel) and total momentum flux (bottom panel) for balloon 01\_STR1. Smaller graphs represent time corresponding zooms of the curves. Note the gaps in the timeseries, which correspond to balloon depressurization events.

140 In the following, we will use two different intrinsic-frequency bands. The wide frequency  
 141 range (WF) corresponds to intrinsic periods between 15 min and 1 day, and includes a  
 142 broad range of gravity-wave frequencies. The high-frequency range (HF), on the other hand,  
 143 provides a focus on intrinsic periods between 15 and 60 min, and is associated with high-  
 144 frequency waves that propagate nearly vertically in the atmosphere (Preusse et al., 2008).  
 145 Note that the high-frequency limit of each band has been chosen to avoid concerns with  
 146 either the balloon oscillations about its equilibrium density level (which occur at  $\hat{\omega}_b \sim N$ )  
 147 with  $\hat{\omega}_b$  the balloons natural frequencies, or the balloon tendency to depart from a perfect  
 148 isopycnic behavior when disturbed by high-frequency waves (Vincent & Hertzog, 2014).

149 Figure 2 displays timeseries of the variances of temperature and vertical velocity, and  
 150 of the total momentum flux for balloon 01\_STR1. The blue curve corresponds to the con-  
 151 tribution of WF waves, whereas the red curve represents the contribution of HF waves.  
 152 The temperature variance timeseries highlight the strong contrast in the behavior of the  
 153 WF and HF components: the contribution of high-frequency waves to the total variance  
 154 of temperature fluctuations accounts only for a very small fraction. This contrast is in  
 155 agreement with the  $\sim \hat{\omega}^{-2}$  scaling of gravity-wave temperature fluctuations in the lower  
 156 stratosphere, which implies that waves with long-intrinsic periods are responsible for most  
 157 of the temperature variance (Podglajen et al., 2016, 2020). Note also that sporadic events  
 158 are responsible for most of the variations in the HF temperature variance timeseries.  
 159 The vertical-velocity variance timeseries exhibits an opposite picture: high-frequency waves  
 160 are this time almost entirely responsible for the total variance. This is consistent with the  
 161 nearly flat intrinsic-frequency spectrum of the vertical wind (Podglajen et al., 2016). A  
 162 second major difference is associated with the variability (or intermittency) present in the  
 163 vertical-velocity timeseries. Sporadic events can induce short, local peaks of vertical-velocity  
 164 variance one order of magnitude larger than the baseline, which are responsible for the large  
 165 tails of the probability distribution of vertical velocity described in (Podglajen et al., 2016).

166 The total momentum flux timeseries displays an intermediate behavior between those two  
 167 extremes as it results from the product of the vertical velocity with the wind horizontal com-  
 168 ponent, which scales as  $\hat{\omega}^{-2}$  like the temperature. This intermediate behavior corresponds  
 169 to the  $\sim \hat{\omega}^{-1}$  scaling of the momentum-flux spectrum (Hertzog et al., 2008; Podglajen et  
 170 al., 2020). The intermittent character of momentum fluxes is observed in both the HF and

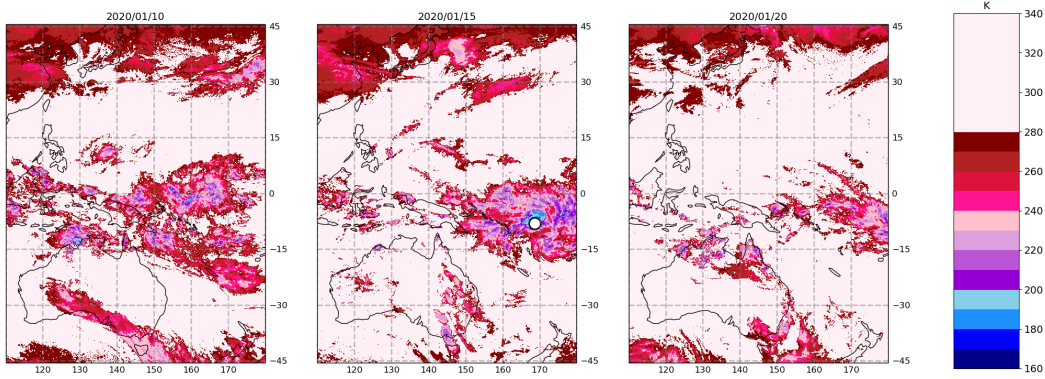


Figure 3: Maps of infrared brightness temperatures between January 10<sup>th</sup> and January 20<sup>th</sup>, 2020. Balloon 01\_STR1 location on January 15<sup>th</sup> is shown with a white circle on the middle map.

171 WF contributions, even though HF waves contribute to only  $\sim 1/3$  of the total momentum  
 172 flux (see also Table 2). We will show in the rest of the study that the peaks in wave activity  
 173 occur when balloons are flying over deep convective systems.

## 174 2.2 Infrared brightness temperatures

175 To locate Strateole-2 balloons with respect to deep convective systems, we have used  
 176 the NOAA/NCEP GPM\_MERGIR product. This product consists in merged images of  
 177 brightness temperature in the atmospheric window (at  $\sim 11 \mu\text{m}$ ) provided by European,  
 178 Japanese, and U.S. geostationary satellites (Meteosat, Indoex, Himawari, GOES-W, and  
 179 GOES-E). The product is available with a spatial and temporal resolution of 4 km and  
 180 30 min, respectively (Janowiak et al., 2017). To reduce the number of images to be pro-  
 181 cessed and as an hourly resolution was sufficient for our purposes, we have averaged pairs  
 182 of successive satellite images.

183 Timeseries of distance between balloons and convection has been computed from these  
 184 brightness temperature images. First, the raw balloons 30-s timeseries were averaged at the  
 185 same hourly resolution as the satellite images. Then, the distance between the balloon and  
 186 the closest pixel with a brightness temperature lower than 235 K was defined as the balloon  
 187 distance to the nearest convective system. Sensitivity tests performed on the threshold  
 188 brightness temperature ( $\pm 5$  K difference) did not show any significant impact on the results  
 189 presented in the following sections.

190 As a simpler proxy for the influence of underlying convective systems, we have also used  
 191 the infrared brightness temperature directly below the balloons. The results obtained this  
 192 way, though generally in agreement with those obtained with the distance to convection,  
 193 are noisier. Convective gravity waves may actually propagate slantwise in the atmosphere,  
 194 and the distance to convection therefore seems a wiser proxy to determine whether the wave  
 195 activity in the balloon timeseries has a convective origin.

## 196 3 A case study

197 In this section, we use a case study to illustrate the treatment done on the balloon  
 198 and brightness temperature datasets. The wave event took place in the Western Pacific  
 199 Ocean ( $\sim 170^\circ\text{E}$ ,  $5^\circ\text{S}$ ) to the east of Solomon Islands, on January 15<sup>th</sup>, 2020. Figure 3  
 200 displays maps of infrared brightness temperatures over 10 days centered on the event. The  
 201 position of balloon 01\_STR1 that recorded the event is displayed in the middle map. The

202 maps illustrate the eastward propagation of a large-scale convective complex in the course of  
 203 these 10 days. This complex is related to an active phase of a Madden-Julian Oscillation  
 204 event (Zhang & Mu, 2005; Madden & Julian, 1971, 1972). The convection is particularly  
 205 active on January 15<sup>th</sup>, and balloon 01\_STR1 is flying over the center of the convective area  
 206 on that day.

207 Figure 4 presents a zoom on the convective complex from January 14<sup>th</sup> 19 UT to Janu-  
 208 ary 15<sup>th</sup> 23 UT. The beginning of this 1-day time period, which corresponds to the morning  
 209 (6 LT to 12 LT), is characterized by the development of several isolated convective systems  
 210 within the complex. Most of these systems progressively dissipate during the afternoon.  
 211 Yet, a system located in the center of the convective complex, right below balloon 01\_STR1  
 212 position, intensifies from mid-afternoon (15 LT) on to the sunset (18 LT). Shortly after,  
 213 the convection is re-activated over the whole complex, producing a wide area of brightness  
 214 temperatures below 200 K. Whatever the time during that day, balloon 01\_STR1 remains  
 215 within 4km from a ‘convective’ pixel, i.e. less than a pixel away from brightness tempera-  
 216 tures lower than 235 K.

217 The sunset and the wide area of low infrared flux are the reasons that cause balloon 01\_STR1  
 218 to depressurize for 10 hours. The corresponding period is shown with red-framed maps in  
 219 Figure 4. The balloon records associated with the depressurization event are discarded from  
 220 our analysis.

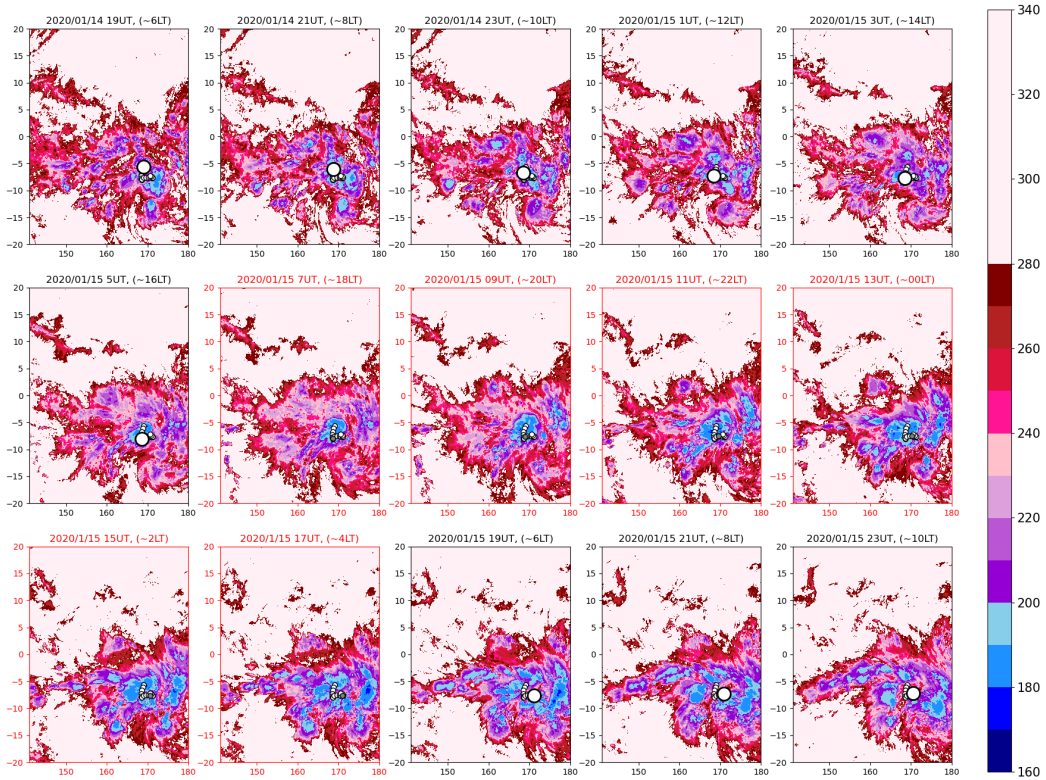


Figure 4: Same as Figure 3, but from January 14<sup>th</sup> 20 UT to January 15<sup>th</sup> 20 UT. The large white circle on each map represents balloon 01\_STR1 position at the corresponding date and time. The lower white circles show the balloon trajectory during this 1-day period. Maps with red axes and title correspond to the time period during which the balloon depressurized. In those maps, the balloon position is indicated with a small grey circle, distance to convection was less than 4 km all along.

Figure 5 displays the total WF and HF components of the gravity-wave momentum flux estimated from balloon 01\_STR1 observations over a 30-hr period centered on January 15<sup>th</sup>, 2020. Missing data in this figure are associated to the depressurization of balloon 01\_STR1. Both momentum flux timeseries exhibit a marked increase after 02 UT (13 LT) on January 15<sup>th</sup>. This timing corresponds to the development of the convective system in the center of the convective complex. The WF momentum flux typically undergoes a variation of one to two orders of magnitude, with a peak value over 120 mPa. More than half of this increase is accounted for by high-frequency waves, which vary by two orders of magnitude. In agreement with Lane et al. (2001), this increase in momentum fluxes seems to correspond to the developing phase of the convective system. In particular, momentum fluxes associated with both frequency ranges exhibit some decrease just before the balloon depressurization, at which stage the convective system is more mature and apparently less prone to trigger gravity waves (Stephan & Alexander, 2015). This decrease is even more drastic in the high-frequency component. Momentum flux values estimated right after the balloon has pressurized back (at sun rise) are similar to those observed prior to the peak, despite the large area of low brightness temperatures that remains at that time (see 18 UT, 7 LT on January 15<sup>th</sup> in Figure 4). Of course though, one can not rule out other episodes of increased momentum flux during the balloon depressurization. We finally notice that the hourly-resolution of momentum fluxes (dots in Figure 5) is sufficient to represent the major variation of this wave event given the frequency range under investigation. Those averaged momentum fluxes are used in the next section in association with distances to convection to quantify statistically the relation between momentum fluxes and distance to convection. The oceanic convective event depicted in this case study illustrates the complexity associated with the organization of tropical convection. Regarding gravity-wave generation, superpressure balloons observations collected in the direct vicinity of such systems therefore provide a quantitative assessment of gravity-wave activity that complement numerical simulations, which tend to address more idealized situations (Lane et al., 2001; Lane & Shaman, 2006; Lane & Zhang, 2011). Note that the case study depicted here corresponds to the largest momentum-flux event identified during the 8 balloon flights of the 2019 Stratoole-2 campaign. About five events with momentum-flux values larger than 60 mPa have been identified in those flights. Events associated with values lower than 40 mPa are, on the other hand, more common (see next Section). This event was chosen to illustrate a clear event of convectively generated waves, with the balloon located right above the convective area, together with an episode of depressurization. Those depressurization events altogether represent less than 5% of the data.

## 4 Statistical results

We now statistically examine the whole 30-s dataset recorded during the eight flights of the 2019 campaign. Timeseries associated with STR and TTL balloons have been treated altogether, after careful examination that the differences between flights were not attributable to physical factors (e.g., different flight levels), but resulted from different sampling of the tropical area. This is illustrated by the summary statistics for each flight given in Table 2.

Figure 6 shows boxplots of total momentum fluxes for WF and HF waves displayed with respect to the balloon distance to convection. The distance bins have been chosen to ensure a minimum number of 300 observations per bin to reduce the noise in the distribution tails, and with a finest resolution of 25 km. The most prominent feature exhibited by these boxplots is the monotonic decrease of gravity-wave momentum fluxes as distance to convection increases. This is a clear confirmation that deep convection constitutes the main source of gravity waves in the tropics (Alexander & Pfister, 1995; Lane et al., 2001; Ern et al., 2004; Alexander et al., 2008). One can also notice that this decrease is steeper for high-frequency waves than for waves with longer frequencies. Whereas mean momentum fluxes associated with HF waves differ by a factor  $\sim 5$  when observations are performed within 25 km or 1,000 km away from a convective system, momentum fluxes associated

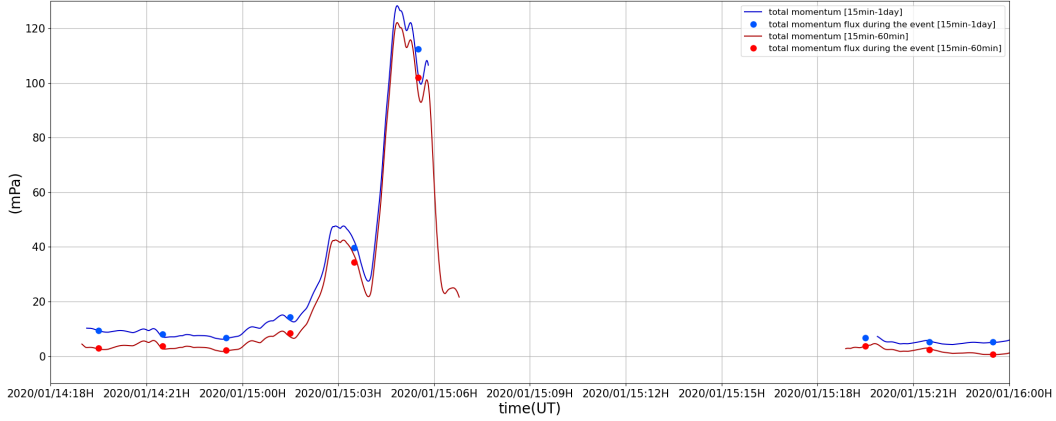


Figure 5: Gravity-wave total momentum flux estimated from balloon 01\_STR1 observations around January 15<sup>th</sup>, 2020. Dots on each curve represent the hourly-averaged momentum flux associated with maps shown in Figure 4.

273 with WF waves vary only by a factor  $\sim 2.5$ . This differential variation is likely linked to  
 274 the fact that high-frequency waves propagate almost vertically in the atmosphere, and are  
 275 thus preferentially observed close to their source in the lower stratosphere. On the other  
 276 hand, the more oblique propagation of longer waves enables them to be observed farther  
 277 away from their source region. Other sources than convection may also contribute to the  
 278 observed background gravity-wave activity.

279 The other striking feature of momentum fluxes displayed in Figure 6 is the inter-quartile  
 280 range between the 10<sup>th</sup> to 90<sup>th</sup> quantiles in each distance bin. This range expresses how  
 281 widely momentum fluxes may vary when observations are performed at a given distance  
 282 from convection. Figure 6 shows that gravity-wave momentum fluxes are significantly more  
 283 variable close to convection than farther away. This is even more conspicuous for the higher  
 284 frequency waves considered in this study: in the 15 min - 60 min frequency band, the 10<sup>th</sup>  
 285 quantile hardly varies with the distance of the balloon to convection, whereas the 90<sup>th</sup>  
 286 percentile undergoes a factor  $\sim 5$  variation. This statistical increase in the range of momentum  
 287 fluxes close to convection has been already noted in the previous section: it is likely linked  
 288 to the preferred generation of gravity waves at specific stages of the convection life cycle  
 289 and/or filtering of directional propagation. The intermittent nature of convective gravity  
 290 waves is also illustrated in Figure 6 by the larger departure close to convection between the  
 291 mean and median momentum fluxes in each distance bin.

292 Last, it is also interesting to note that at a distance of more than 300 – 400 km away from  
 293 convective systems, momentum fluxes associated with gravity waves in the tropical lower  
 294 stratosphere look rather constant (typically 3 mPa for 15 min - 1 day waves), which would  
 295 support some background values in gravity-wave drag parameterizations.  
 296

297 The lowest panel of Figure 6 displays the number of observations per bin of distance to  
 298 convection. This panel emphasizes how often the balloons were located close to convective  
 299 systems during the 2019 campaign: observations were collected less than 200 km away from  
 300 convection more than half of the time (53%), and less than 50 km away more than a quarter  
 301 of the time (26%).

302 To further exemplify the relation of tropical gravity waves to convection, we show in  
 303 Figure 7 the reverse distribution: boxplots of distance to convection with respect to WF-  
 304 and HF-wave momentum fluxes. As previously, we have ensured a minimum number of  
 305 300 observations per bin. The figure clearly illustrates that the largest momentum fluxes

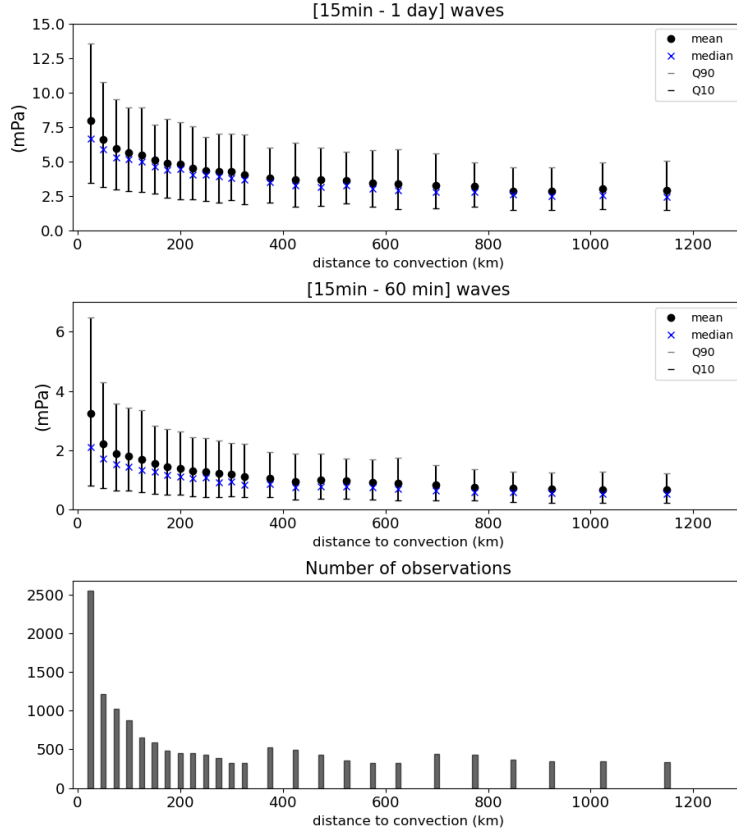


Figure 6: Boxplots of total momentum fluxes associated with (top) WF waves and (middle) HF waves with respect to the balloon distance to convection. In both panels, the mean, median, as well as the 10<sup>th</sup> and 90<sup>th</sup> quantiles in each bin are presented. (Bottom) Number of observations within each distance bin.

306 (> 5 mPa) are only recorded when the balloons are located at short distances from convective  
 307 systems, typically less than 400 km away. In contrast, and as previously noticed, lower  
 308 momentum fluxes are generally associated with larger distances to convective systems, but  
 309 may also be observed sometimes in the vicinity of such systems. Note yet that the smallest  
 310 momentum fluxes (< 2 mPa for WF waves, and < 0.5 mPa for HF waves) are not observed  
 311 in the direct proximity of convection. Those two figures have hence demonstrated that a  
 312 short distance to convective systems is a necessary, but not sufficient condition to observe  
 313 large gravity-wave momentum fluxes in the tropical lower stratosphere. In other words,  
 314 convection is the most prominent gravity wave source in the tropics, but the generation  
 315 process is intermittent.

316 We finally display in Figure 8 the probability distribution function (pdf) of momentum  
 317 fluxes associated with WF waves. We show the pdf obtained with observations collected  
 318 more than 500 km away from convection, as well as that obtained with observations col-  
 319 lected less than 200 km away from a convective system. The two pdfs differ remarkably  
 320 from each other, the one associated with observations close to convection exhibiting a larger  
 321 tail of large-amplitude wave events, in agreement with previous figures. Jewtoukoff et al.  
 322 (2013) also reported on gravity-wave momentum-flux pdf in the tropical area during the  
 323 Pre-Concordiasi campaign. Despite similar averaged momentum fluxes (i.e., between 4 and  
 324 5 mPa), Jewtoukoff et al. (2013)'s pdfs have significantly longer tails than those obtained  
 325 in this study. In their study, Jewtoukoff et al. (2013) did not remove the balloon depres-

Table 2: Averaged momentum fluxes and temperature variances observed during the Strateole-2 2019 campaign. The all flights line is the time averaged momentum fluxes from all the flights.

Flight	Momentum fluxes (mPa)		Temperature variances ( $K^2$ )	
	15 min - 1 day	15 min - 60 min	15 min - 1 day	15 min - 60 min
01_STR1	5.42	1.97	1.64	0.08
02_STR2	4.88	1.60	1.18	0.04
03_TTL3	5.84	1.92	1.52	0.05
04_TTL1	4.96	1.34	1.31	0.03
05_TTL2	5.99	1.84	1.60	0.04
06_STR1	3.71	1.13	1.35	0.05
07_STR2	4.39	1.36	1.73	0.07
08_STR2	4.28	1.43	1.44	0.04
All flights	5.02	1.62	1.48	0.05

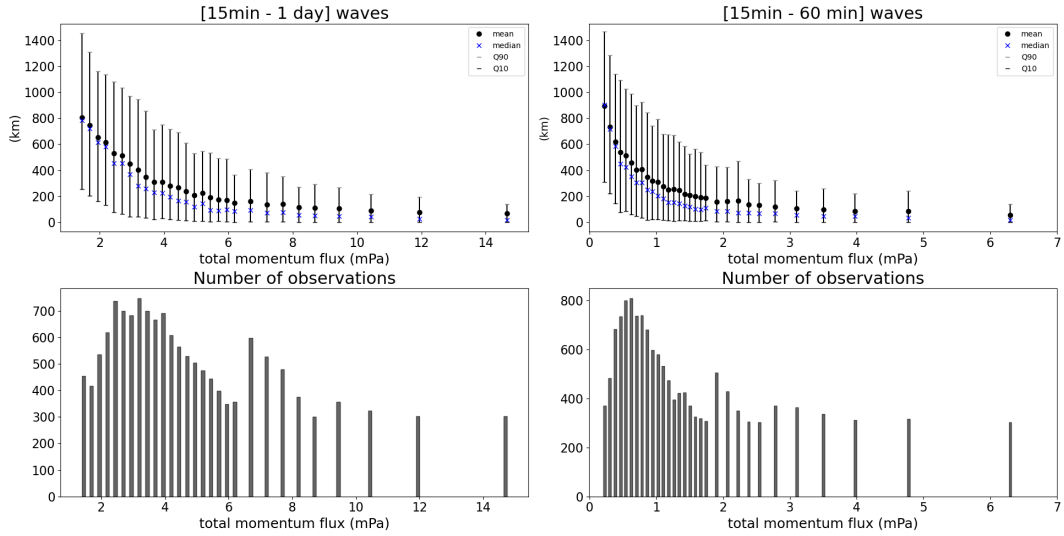


Figure 7: (Top) Boxplots of distance to convection with respect to gravity-wave momentum fluxes associated with (left) WF and (right) HF waves. The same quantities as in Figure 6 are displayed. (Bottom) Number of observations per momentum-flux bin.

326 surization events, unlike what is done here. This difference in treatment may explain the  
 327 observed differences in the pdfs, since depressurization events may be associated with large  
 328 vertical displacements of the balloons. Furthermore, momentum fluxes are overestimated  
 329 during such events as the balloon is no longer isopycnic.

330 For completeness, we also show in Figure 9 boxplots of temperature variances associ-  
 331 ated with gravity-wave disturbances with respect to the balloon distance to convection.  
 332 The general behavior of temperature variances is similar to that of momentum fluxes: larger  
 333 variances are observed closer to convection, and the largest temperature variances (repre-  
 334 sented by the 90th quantiles) are strongly linked to convective systems. Yet, the range of  
 335 variation of the mean temperature variances is significantly smaller than that of momentum  
 336 fluxes: it varies by typically less than a factor 2 for WF waves when the balloon distance

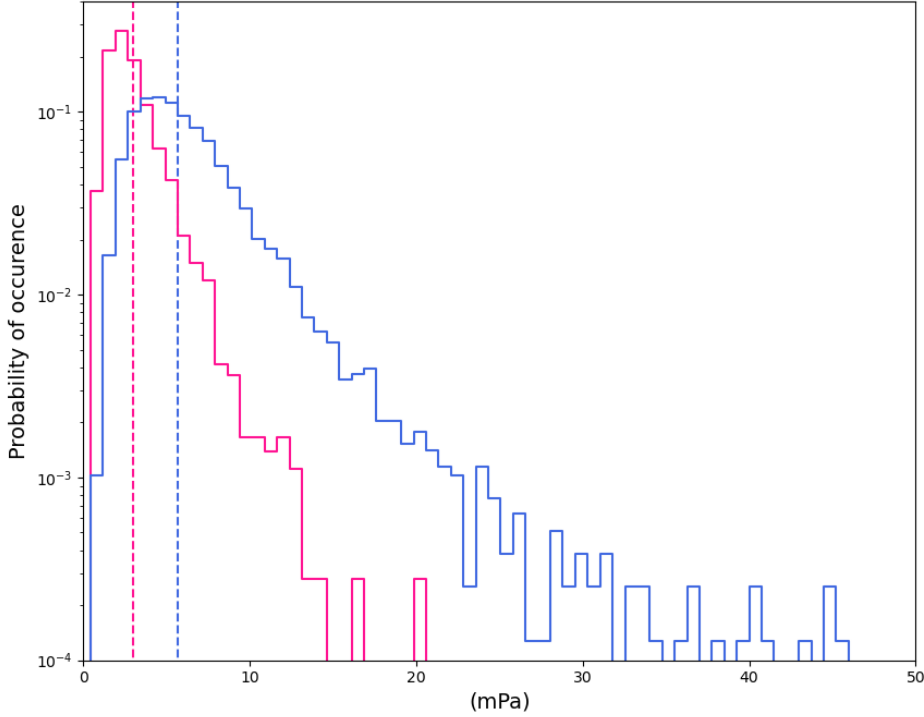


Figure 8: Pdf of momentum flux for WF waves: (pink) observations collected more than 500 km, and (blue) observations collected less than 200 km away from a convective system. Vertical dashed lines represent the corresponding means.

337 to convection changes from 0 to 1,000 km. Values level off to a background value from  
 338 400 km on at  $1.2 \text{ K}^2$  for WF waves. This is reminiscent of timeseries displayed in Figure 2,  
 339 which showed less intermittency in temperature variances than in momentum fluxes. In con-  
 340 trast with momentum fluxes, temperature variances therefore appear less strongly linked to  
 341 gravity-wave sources in the tropical lower stratosphere, which is consistent with the larger  
 342 contribution of low-frequency waves that propagate more horizontally in those variances, as  
 343 discussed in Section 2.

## 344 5 Discussion

### 345 5.1 Ratio between HF and WF waves

It is common to characterize gravity waves in terms of universal spectra. For example, numerous studies have provided evidence that gravity-wave energy scales as  $m^{-3}$ , with  $m$  the vertical wavenumber (Fritts & Alexander, 2003, and references therein). Similarly, long-duration balloon observations have shown that the spectrum of gravity-wave momentum fluxes scales as  $\hat{\omega}^{-s}$  with  $s=1$  (e.g., Hertzog et al., 2008). Such laws imply a constant ratio between different ranges of wavenumbers or frequencies. For instance, the ratio of momentum fluxes associated with WF and HF reads:

$$\frac{\int_{\text{WF}} \overline{u'_{\parallel} w'}(\hat{\omega}) d\hat{\omega}}{\int_{\text{HF}} \overline{u'_{\parallel} w'}(\hat{\omega}) d\hat{\omega}} = \frac{\ln \frac{86400}{900}}{\ln \frac{3600}{900}} \approx 3.3 \quad (4)$$

346 assuming the  $\hat{\omega}^{-1}$  scaling.

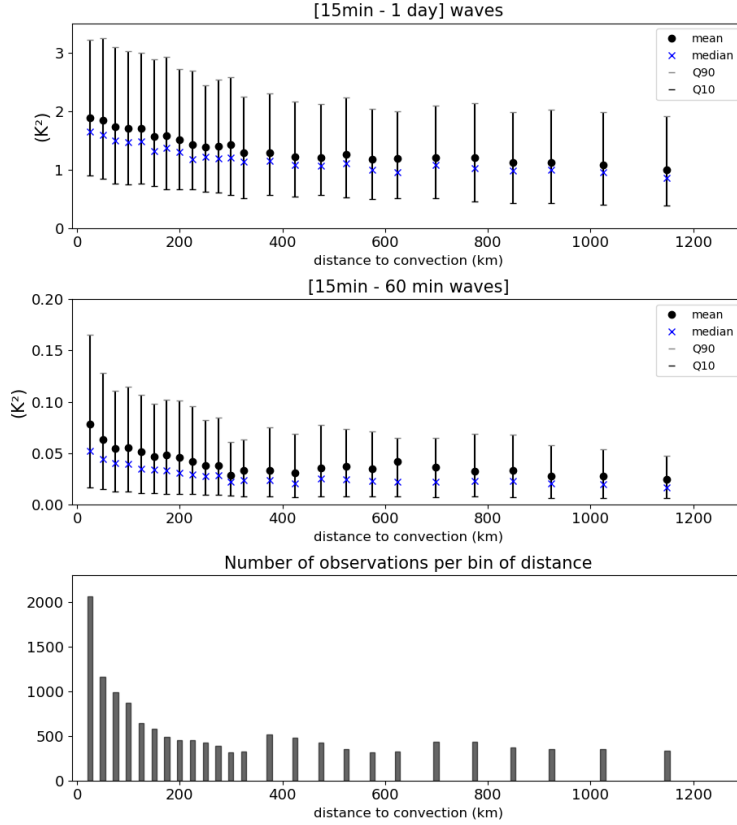


Figure 9: Same as Figure 6, but for gravity-wave temperature variances.

347 Results shown in the previous sections indicate that this ratio is only statistically valid  
 348 in the tropical lower stratosphere. It holds when observations collected over different me-  
 349 teorological situations are averaged altogether. Indeed, Figure 6 for instance shows that  
 350 momentum fluxes associated with HF waves are more sensitive to the distance to convec-  
 351 tion than those associated with WF waves. This result is further explored in Figure 10,  
 352 which displays the ratio of WF- to HF-wave momentum fluxes as a function of the balloon  
 353 distance to convection. It is obvious that this ratio increases as waves observations are  
 354 collected farther away from convection. In other words, short-period waves contribute more  
 355 to the total momentum flux close to convection than they do far away. The momentum-flux  
 356 spectral slope consequently varies by a few percents as well with the proximity to convective  
 357 wave sources, at least in the tropical lower stratosphere. It might well be that this depen-  
 358 dence is lost farther above (when the distance to the wave sources has increased), but this  
 359 remains to be explored. The 3.3 momentum-flux ratio, associated with the  $\hat{\omega}^{-1}$  scaling, thus  
 360 only corresponds to a mean value, which is close to the mean value measured 3.1 during the  
 361 campaign.

## 362 5.2 Geographic distribution of gravity-wave momentum fluxes

363 The previous sections have stressed the link between gravity-wave activity in the tropical  
 364 lower stratosphere and deep convection below. In this section, we report on the associated  
 365 geographic distribution of gravity-wave momentum fluxes in the tropical lower stratosphere.

366 Figure 11 displays maps of WF- and HF-wave momentum fluxes averaged over all flights  
 367 in 20°-longitude bins. The geographical bins encompass the whole 20°S – 15°N latitude

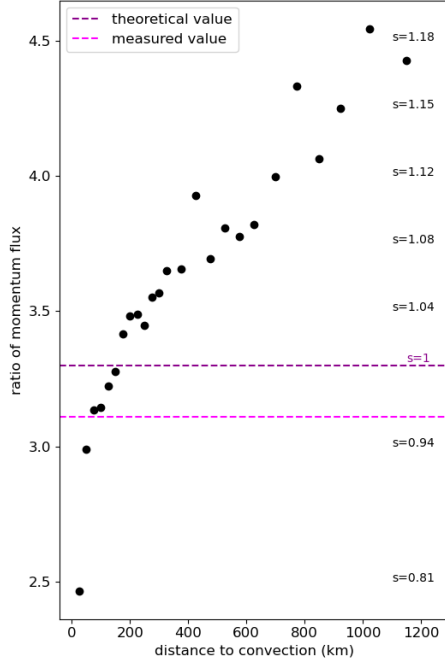


Figure 10: Ratio of WF-wave (15 min–1 day) to HF-wave (15 min–60 min) momentum fluxes as a function of balloon distance to convection. The purple horizontal line shows the ratio associated with the  $\hat{\omega}^{-1}$ -scaling of momentum fluxes. The measured power-law scaling is shown by the pink horizontal line. The correspondence between the WF to HF momentum-flux ratios and the power-law scalings is displayed on the right-hand side of the figure.

368 range sampled by the balloons, since the number of collected observations during the first  
 369 Strateole-2 campaign did not enable us to clearly demonstrate inter-hemispheric differences.  
 370 Both maps highlight a clear contrast between quieter regions (Eastern Pacific Ocean, Eastern  
 371 Atlantic Ocean) and more active regions (South America, Eastern Africa, and the Maritime  
 372 Continent), in agreement with maps from Randel et al. (2021). The amplitude of geographic  
 373 variability is different than that of Randel et al. (2021), but this difference is certainly  
 374 associated with their use of temperature disturbances to study gravity waves, while we have  
 375 chosen momentum fluxes. (Ern & Preusse, 2012) also reported on 20–30% enhancements in  
 376 gravity-wave momentum fluxes over convective regions as compared to non-convective ones.  
 377 The variability of wave momentum fluxes displayed in Figure 11 is somewhat larger, which  
 378 is likely associated with the capability of superpressure balloons to observe higher-frequency  
 379 waves than the High Resolution Dynamics Limb Sounder (HIRDLS) instrument used in Ern  
 380 and Preusse (2012).

381 Momentum fluxes are found generally larger above the continents than above the  
 382 oceans. Yet, the western part of the South Pacific Convergence Zone stands out as the sec-  
 383 ond region with largest wave activity. The convection there was particularly active during  
 384 the campaign, as highlighted in the case study shown previously. The geographic behavior  
 385 of gravity-wave momentum fluxes is in line with properties of tropical convection in the tro-  
 386 posphere: regions associated with larger momentum fluxes are also those where convective  
 387 systems are more prone to overshoot in the upper troposphere (Alcala & Dessler, 2002; Liu  
 388 & Zipser, 2005).

389 WF- and HF-wave maps look very similar, except for a slightly larger decrease in the HF-  
 390 wave momentum fluxes away from the most active regions. The width of the longitude bins

391 used here is indeed too large to capture the differential behavior of short- and long-period  
 392 waves with respect to the convective source that was stressed in the previous sections.  
 393 We finally note the striking west-east monotonic decrease in wave momentum fluxes over  
 394 the Pacific Ocean, and, on the other hand, the relatively uniform distribution of momentum  
 395 fluxes over the Indian Ocean. This latter feature is likely linked to the historically anomalous  
 396 positive event of the Indian Ocean Dipole (IOD) that took place in 2019 (Lu & Ren,  
 397 2020). In a positive IOD phase, equatorial sea surface temperatures in the western Indian  
 398 Ocean are warmer than their climatological values. Such positive IOD phases therefore re-  
 399 duce the climatological positive west-east gradient in convection over the basin (Saji et al.,  
 400 1999; Webster et al., 1999), and thus likely contribute to a more balanced distribution of  
 401 wave activity in that region.

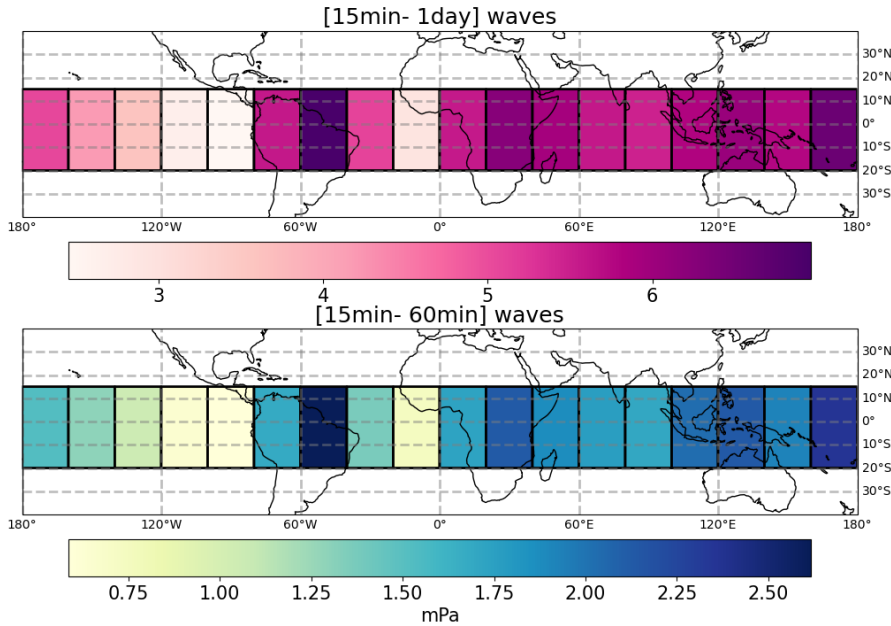


Figure 11: Maps of campaign-mean momentum flux:(top) 15 min–1 day waves, (bottom) 15 min–60 min waves.

Figure 12 shows maps of the contribution of the top 10% momentum-flux events to the mean momentum flux, for both the WF- and HF-bands considered in this study. These contributions are computed as:

$$\frac{\sum_{f_i > f_{q90}} f_i}{\sum_{i=1}^{N_{\text{obs}}} f_i} \times 100 \quad (5)$$

402 where  $f_i$  represents the instantaneous momentum flux integrated in either the WF- or HF-  
 403 frequency band,  $f_{q90}$  the associated 90<sup>th</sup> quantile, and  $N_{\text{obs}}$  the number of observation  
 404 points. Those maps therefore characterize the intermittency of gravity waves in the equa-  
 405 torial lower stratosphere (Alexander et al., 2010; Hertzog et al., 2012; Plougonven et al.,  
 406 2013; Wright et al., 2013).

407 In agreement with the raw timeseries displayed in Figure 2, Figure 12 shows that the  
 408 intermittency associated with the highest-frequency waves is significantly larger than that  
 409 obtained when the full 15 min–1 day band is considered: the top most 10% events con-  
 410 tribute to 30–40% of the mean momentum flux associated with HF waves, whereas their

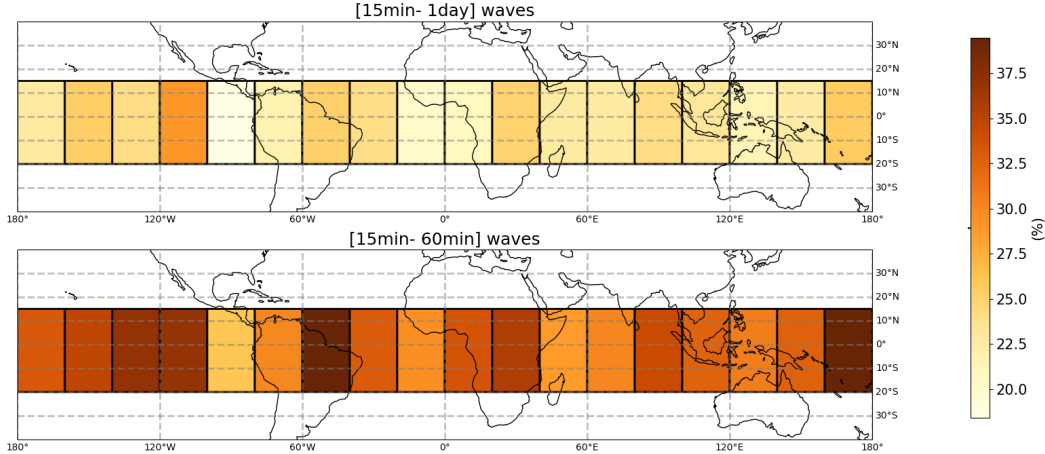


Figure 12: Contribution of the top 10% momentum-flux events to the mean momentum flux: (top) 15 min–1 day waves, (bottom) 15 min–60 min waves.

411 contribution to the WF-wave momentum fluxes is  $\sim 25\%$ . This difference is likely partly  
 412 explained by the rapid decrease of HF-wave momentum fluxes with the distance to the con-  
 413 vective source, which was emphasized in the previous section. But it may also result from  
 414 differences in the range of source mechanisms contributing to different parts of the gravity  
 415 wave spectrum.

416 In general, bins with the largest momentum fluxes are also those with the highest inter-  
 417 mittency. This likely reflects the transient nature of the convective wave source and its  
 418 modulation at a broad range of timescales: the life cycle of convection itself, diurnal cycle,  
 419 equatorial Kelvin or Rossby waves, longer-period MJO events. Yet some interesting  
 420 discrepancies between maps of momentum fluxes and those of intermittency are worth high-  
 421 lighting. The wave intermittency is, for instance, larger around  $120^\circ\text{W}$  than it is nearby.  
 422 Similarly, it is larger over the eastern Indian Ocean than over its western part. We have no  
 423 clear interpretation for these “outliers”, but note that they may result from a combination  
 424 of causes, including a more transient nature of convection in these bins or the result of a  
 425 limited sampling by the 2019 balloon flights. Last, we note that the intermittency values  
 426 reported in this study agree fairly well with those obtained by Wright et al. (2013) and  
 427 Ern et al. (2014) in the tropical lower stratosphere with satellite observations. Hertzog  
 428 et al. (2012) and Wright et al. (2013) reported on much larger figures at higher latitudes,  
 429 where orographic waves represent a significant fraction of the gravity-wave momentum flux.  
 430 There, the top 10% waves may contribute to more than 60% of the mean momentum flux.  
 431 Our study therefore confirms that the intermittency associated with convective waves, while  
 432 obviously present in the balloon dataset, is rather moderate.

### 433 5.3 Gravity-wave contribution to the driving of the QBO

In this following discussion, we intend to provide a rough assessment of the contribution  
 of the gravity waves observed during the balloon campaign to the overall driving of the QBO.  
 For this, we start from a simplified version of the Transformed Eulerian Mean equation for  
 zonal momentum (Andrews et al., 1987):

$$\rho \left( \frac{\partial \bar{u}}{\partial t} + \bar{w}^* \frac{\partial \bar{u}}{\partial z} \right) = - \frac{\partial \overline{\rho u' w'}}{\partial z} \quad (6)$$

434 where  $\bar{u}$  is the zonal-mean zonal wind, and  $\bar{w}^*$  is the residual vertical velocity. In Equa-  
 435 tion (6), we have followed Alexander and Ortland (2010) and have neglected the meridional

436 advection term. This primarily stems from the fact that the QBO is essentially symmetric  
 437 about the equator, and that the Coriolis force is small at low latitudes: more than 80%  
 438 of the balloon observations have actually been recorded within  $10^\circ$  of the equator. Ern et  
 439 al. (2014) and Pahlavan et al. (2021) have further examined the tropical stratosphere mo-  
 440 mentum budget in the European Centre for Medium-range Weather Forecasts (ECMWF)  
 441 reanalyses ERA-Interim and ERA-5 reanalyses, respectively. They both suggest that the  
 442 meridional advection term is indeed very weak during westerly-to-easterly QBO transitions,  
 443 which was the configuration during the balloon campaign.

Integrating (6) from the balloon flight level ( $z_{\text{bal}}$ ) to the QBO top altitude ( $z_{\text{top}}$ ) yields:

$$\overline{\rho u'w'}(z_{\text{bal}}) - \overline{\rho u'w'}(z_{\text{top}}) = \int_{z_{\text{bal}}}^{z_{\text{top}}} \rho \left( \frac{\partial \bar{u}}{\partial t} + \bar{w}^* \frac{\partial \bar{u}}{\partial z} \right) dz \quad (7)$$

Noting  $\frac{d\bar{u}}{dt}$  the total zonal-wind acceleration (i.e. the term within parentheses under the  
 integral in (7)), and assuming that most momentum flux has been dissipated at the QBO  
 top altitude, one can use the mean value theorem for definite integrals to obtain:

$$\begin{aligned} \overline{u'w'}(z_{\text{bal}}) &= \frac{d\bar{u}}{dt}(z^*) \int_{z_{\text{bal}}}^{z_{\text{top}}} \rho dz \\ &= \frac{d\bar{u}}{dt}(z^*) \left[ 1 - \exp\left(-\frac{z_{\text{top}} - z_{\text{bal}}}{H}\right) \right] H \end{aligned} \quad (8)$$

444 where  $H \approx 6$  km is the density scale height for a background temperature of 210 K typical  
 445 of the tropical lower stratosphere, and  $z^*$  is an altitude such that  $z_{\text{bal}} < z^* < z_{\text{top}}$ . In the  
 446 tropical lower stratosphere, the absolute value of the total zonal wind acceleration reaches  
 447 up to to 0.5 m/s/day in QBO easterly shear zones (Alexander et al., 2010; Ern et al., 2014;  
 448 Pahlavan et al., 2021). Such accelerations are preferentially found above  $\sim 25$  km, and  
 449 generally occupy less than half of the QBO altitude range (Pahlavan et al., 2021). We thus  
 450 use  $\frac{d\bar{u}}{dt}(z^*) = 0.5$  m/s/day as a maximum value for the density-weighted total acceleration,  
 451 and half of this as a more probable estimate, yet likely still an upper bound.

By conveniently choosing  $z_{\text{top}} = z_{\text{bal}} + 10$  km, one gets an estimate of the needed flux to  
 drive the QBO:

$$\overline{\rho u'w'}(z_{\text{bal}}) \approx 2.8 - 5.6 \text{ mPa} \quad (9)$$

452 Now, the 15 min $-$ 1 day absolute gravity-wave momentum flux estimated from the balloon  
 453 observations is  $\sim 5$  mPa (see Table 2). Of this total, 1.4 mPa correspond to westward fluxes,  
 454 so that 15 min $-$ 1 day waves are responsible for at least 25%, and more probably over 50%,  
 455 of the required flux to drive the QBO above 20 km of altitude during the balloon campaign.  
 456 This estimate is in agreement with e.g., Kawatani et al. (2010) who stressed the primary  
 457 role of gravity waves in driving the descent of QBO easterlies.

## 458 6 Summary and Conclusion

459 Tropical gravity waves have been studied from the observations collected during the  
 460 eight balloon flights of the first Strateole-2 campaign, which took place from November 2019  
 461 to February 2020. The quasi-Lagrangian nature of the superpressure balloons provides direct  
 462 access to the intrinsic frequencies of the waves observed, and allows an accurate estimation  
 463 of the associated momentum fluxes. The main focus of the study was on the relation  
 464 between gravity wave momentum fluxes and the presence of deep convection nearby. Deep  
 465 convection was diagnosed from geostationary satellite images of brightness temperature, and  
 466 the observations were sorted using a simple criterion: the distance from the balloon to the  
 467 nearest convective system, identified as brightness temperatures lower than 235 K.

468 The spectrum of gravity waves considered in the analysis consisted of motions with  
 469 intrinsic periods ranging from 15 minutes, about three times the buoyancy period, to one

470 day. Periods shorter than 15 minutes were not considered so as to avoid effects due to  
 471 the balloon natural oscillations (Podglajen et al., 2016). The campaign-averaged gravity-  
 472 wave momentum fluxes is 5 mPa, and the observed maximum value reaches 120 mPa, on a  
 473 timescale of a couple of hours. In complement to this broad frequency range, a subrange of  
 474 high frequencies (intrinsic periods from 15 to 60 minutes) was considered. The campaign-  
 475 average momentum flux for these high frequencies is 1.61 mPa, about 32% that of the broad  
 476 frequency range, emphasizing their importance.

477 When momentum fluxes are sorted according to the distance to convection, a very clear  
 478 dependence is found. Gravity-wave momentum fluxes show both larger values and greater  
 479 variability close to convection: 90% of the momentum fluxes larger than the mean are  
 480 typically found at distances closer than 400 km from convection (see Figure 7). Conversely,  
 481 momentum fluxes recorded at distances further away than 600 km from convection have  
 482 more than 90% of chance of being lower than the mean (see Figure 6). These results clearly  
 483 confirm that convection is the main source of gravity waves in the tropics.

484 The relation between momentum fluxes and convection is more pronounced for the  
 485 highest frequency waves. The decay of the momentum fluxes at larger distances from con-  
 486 vection is faster for HF waves than it is for WF waves, and far away from convection, the  
 487 HF-wave momentum fluxes tend to a very small value ( $\sim 0.6$  mPa). This contrasts with WF  
 488 waves, for which momentum fluxes tend to a 'background' value of about 3 mPa far away  
 489 from convection. The larger spatial scales and more horizontal propagation of WF waves  
 490 leads to looser relation to the convective sources. The greater contrast for HF waves between  
 491 the vicinity of convection and regions remotely distant from all convection also translates  
 492 in a large intermittency for these HF waves: their 10% highest values contribute to 40% of  
 493 their momentum fluxes. This intermittency is weaker nonetheless than for mountain waves  
 494 at higher latitudes. Convective sources are numerous and the observed samples were most  
 495 often close to convection: more than 50% of time closer than 200 km. The intermittency  
 496 and the relative contributions of HF to WF are consistent with the  $-1$  slope in intrinsic  
 497 frequency found for gravity wave momentum fluxes (Podglajen et al., 2016). Whereas the  
 498 notion of a universal spectrum is valid for the average over all flights, or for long enough  
 499 portions of flights, its relevance for shorter portions of flights should be more nuanced. This  
 500 was illustrated by quantifying the ratio of the HF and WF contributions depending on dis-  
 501 tance to convection. A clear dependence was found, consistently showing greater weight of  
 502 HF waves near convection (up to 40% of the momentum fluxes), and weaker weight far from  
 503 convection (HF waves only account for about 22% of fluxes at  $\sim 1000$  km or more).

504 In contrast to momentum fluxes, temperature fluctuations show much less intermit-  
 505 tency. Their spectrum has a  $-2$  slope in intrinsic frequency, implying a much greater  
 506 weight of low frequency waves. The overall average of temperature variances was  $1.48 \text{ K}^2$   
 507 for the whole spectrum of waves, with the average for HF waves only reaching  $0.05 \text{ K}^2$ . This  
 508 is 29.6 times less than the total variance, consistent with the 31.7 ratio expected for a  $-2$   
 509 spectrum. Temperature variances nonetheless also show a clear sensitivity to distance to  
 510 convection, but with a less pronounced decay, and relatively larger background values found  
 511 at large distances from convection (see Figure 9).

512 The dataset from this first Strateole-2 campaign has allowed a first exploration of grav-  
 513 ity wave momentum fluxes in the lower stratosphere and of their relation to the surrounding  
 514 flow. Directions to pursue include consideration of a more integrative diagnostic for con-  
 515 vection nearby, accounting for the time development of convection and for the direction  
 516 of the shear between the convection and the balloons. Upcoming Strateole-2 campaigns,  
 517 with 20 balloons each planned for 2021-2022 and 2024-2025, will allow us to investigate  
 518 and quantify convectively generated gravity waves over an even wider sample of events and  
 519 configurations.

$$\frac{d\zeta'_b}{dt} = w' \quad (10)$$

## 520 Acknowledgments

521 The balloon-borne TSEN data were collected as part of Strateole-2, which is sponsored  
522 by CNES, CNRS/INSU, NSF, and ESA. The Strateole-2 TSEN dataset is available at  
523 <https://data.ipsl.fr/catalog/strateole2/>.

524 The merged IR satellite images were collected from the NOAA/NCEP GPM\_MERGIR prod-  
525 uct, available at [https://disc.gsfc.nasa.gov/datasets/GPM\\_MERGIR\\_1/summary](https://disc.gsfc.nasa.gov/datasets/GPM_MERGIR_1/summary). Martina  
526 Bramberger and Joan Alexander are warmly thanked for thoughtful discussions and sug-  
527 gestions during the final stage of the paper. This study was supported by ANR Booster.  
528 Milena Corcos is funded through a Sorbonne-Universite and CNES doctoral fellowship. No  
529 author declare any conflict of interest.

## 530 References

- 531 Alcala, C. M., & Dessler, A. E. (2002). Observations of deep convection in the tropics using  
532 the Tropical Rainfall Measuring Mission (TRMM) precipitation radar. *J. Geophys.*  
533 *Res.*, *107*, 17-1–17-7. doi: 10.1029/2002JD002457
- 534 Alexander, M. J., Geller, M., McLandress, C., Polavarapu, S., Preusse, P., Sassi, F., ...  
535 Watanabe, S. (2010). Recent developments in gravity-wave effects in climate models  
536 and the global distribution of gravity-wave momentum flux from observations and  
537 models. *Qu. J. Roy. Meteor. Soc.*, *136*, 1103–1124. doi: 10.1002/qj.637
- 538 Alexander, M. J., Gille, J., Cavanaugh, C., Coffey, M., Craig, C., Eden, T., ... Dean,  
539 V. (2008). Global estimates of gravity wave momentum flux from High Resolution  
540 Dynamics Limb Sounder observations. *J. Geophys. Res.*, D15S18. doi: 10.1029/  
541 2007jd008807
- 542 Alexander, M. J., Holton, J. R., & Durran, D. R. (1995). The Gravity Wave Response  
543 above Deep Convection in a Squall Line Simulation. *J. Atmos. Sci.*, *52*, 2212–2226.  
544 doi: 10.1175/1520-0469(1995)052<2212:TGWRAD>2.0.CO;2
- 545 Alexander, M. J., & Ortland, D. A. (2010, dec). Equatorial waves in High Resolution  
546 Dynamics Limb Sounder (HIRDLS) data. *J. Geophys. Res.*, *115*(D24). doi: 10.1029/  
547 2010jd014782
- 548 Alexander, M. J., & Pfister, L. (1995). Gravity wave momentum flux in the lower strato-  
549 sphere over convection. *Geophys. Res. Lett.*, *22*, 2029–2032. doi: 10.1029/95GL01984
- 550 Andrews, D. G., Holton, J. R., & Leovy, C. B. (1987). *Middle atmosphere dynamics*.  
551 Academic Press.
- 552 Baldwin, M. P., Gray, L. J., Dunkerton, T. J., Hamilton, K., Haynes, P. H., Randel, W. J.,  
553 ... Takahashi, M. (2001). The quasi-biennial oscillation. *Rev. Geophys.*, *39*, 179–229.  
554 doi: 10.1029/1999RG000073
- 555 Boccara, G., Hertzog, A., Vincent, R. A., & Vial, F. (2008). Estimation of Gravity  
556 Wave Momentum Flux and Phase Speeds from Quasi-Lagrangian Stratospheric Bal-  
557 loon Flights. Part I: Theory and Simulations. *J. Atmos. Sci.*, *65*, 3042-3055. doi:  
558 10.1175/2008JAS2709.1
- 559 Butchart, N., Anstey, J. A., Hamilton, K., Osprey, S., McLandress, C., Bushell, A. C.,  
560 ... Yukimoto, S. (2018). Overview of experiment design and comparison of models  
561 participating in phase 1 of the SPARC Quasi-Biennial Oscillation initiative (QBOi).  
562 *Geosci. Model Dev.*, *11*, 1009–1032. doi: 10.5194/gmd-11-1009-2018
- 563 Dhaka, S. K., Bhatnagar, R., Shibagaki, Y., Hashiguchi, H., Fukao, S., Kozu, T., & Panwar,  
564 V. (2011, dec). Characteristics of gravity waves generated in a convective and a non-  
565 convective environment revealed from hourly radiosonde observation under CPEA-II  
566 campaign. *Ann. Geophys.*, *29*(12), 2259–2276. doi: 10.5194/angeo-29-2259-2011

- 567 Dinh, T., Podglajen, A., Hertzog, A., Legras, B., & Plougonven, R. (2016). Effect of  
568 gravity wave temperature fluctuations on homogeneous ice nucleation in the tropical  
569 tropopause layer. *Atmos. Chem. Phys.*, *16*, 35–46. doi: 10.5194/acp-16-35-2016
- 570 Dunkerton, T. J., & Dunkerton, T. J. (1997). The role of gravity waves in the quasi-biennial  
571 oscillation. *J. Geophys. Res.*, *102*, 26053–26076. doi: 10.1029/96JD02999
- 572 Ern, M., Ploeger, F., Preusse, P., Gille, J. C., Gray, L. J., Kalisch, S., ... Riese, M.  
573 (2014). Interaction of gravity waves with the QBO: A satellite perspective. *Journal*  
574 *of Geophysical Research: Atmospheres*, *119*, 2329–2355. doi: 10.1002/2013jd020731
- 575 Ern, M., & Preusse, P. (2012). Gravity wave momentum flux spectra observed from satellite  
576 in the summertime subtropics: Implications for global modeling. *Geophys. Res. Lett.*,  
577 *39*(15). doi: 10.1029/2012gl052659
- 578 Ern, M., Preusse, P., Alexander, M. J., & Warner, C. D. (2004). Absolute values of  
579 gravity wave momentum flux derived from satellite data. *J. Geophys. Res.* doi:  
580 10.1029/2004jd004752
- 581 Ern, M., Preusse, P., Gille, J. C., Hepplewhite, C. L., Mlynczak, M. G., Russell, J. M., &  
582 Riese, M. (2011). Implications for atmospheric dynamics derived from global obser-  
583 vations of gravity wave momentum flux in stratosphere and mesosphere. *J. Geophys.*  
584 *Res.* doi: 10.1029/2011jd015821
- 585 Ern, M., Preusse, P., Krebsbach, M., Mlynczak, M. G., & Russell, J. M. (2008). Equatorial  
586 wave analysis from SABER and ECMWF temperatures. *Atmos. Chem. Phys.*, *8*,  
587 845–869. doi: 10.5194/acp-8-845-2008
- 588 Fritts, D. C. (1993). Gravity Wave Sources, Source Variability and Lower and Middle  
589 Atmosphere Effects. In E. V. Thrane, T. A. Blix, & D. C. Fritts (Eds.), *Coupling*  
590 *processes in the lower and middle atmosphere* (pp. 191–208). Springer Netherland.  
591 doi: 10.1007/978-94-011-1594-0\_13
- 592 Fritts, D. C., & Alexander, M. J. (2003). Gravity wave dynamics and effects in the middle  
593 atmosphere. *Rev. Geophys.*, *41*, 3-1–3-64. doi: 10.1029/2001RG000106
- 594 Fueglistaler, S., & Baker, M. B. (2006). A modelling study of the impact of cirrus clouds  
595 on the moisture budget of the upper troposphere. *Atmos. Chem. Phys.*, 1425–1434.  
596 doi: 10.5194/acp-6-1425-2006
- 597 Haase, J., Alexander, M. J., Hertzog, A., Kalnajs, L., Deshler, T., Davis, S., ... Venel, S.  
598 (2018). Around the World in 84 Days. *EOS*. doi: 10.1029/2018eo091907
- 599 Hertzog, A., Alexander, M. J., & Plougonven, R. (2012). On the Intermittency of Gravity  
600 Wave Momentum Flux in the Stratosphere. *J. Atmos. Sci.*, *69*, 3433–3448. doi:  
601 10.1175/JAS-D-12-09.1
- 602 Hertzog, A., Basdevant, C., Vial, F., & Mechoso, C. R. (2004). The accuracy of stratospheric  
603 analyses in the northern hemisphere inferred from long-duration balloon flights. *Qu.*  
604 *J. Roy. Meteor. Soc.*, *130*, 607–626. doi: https://doi.org/10.1256/qj.03.76
- 605 Hertzog, A., Boccara, G., Vincent, R. A., Vial, F., & Cocquerez, P. (2008). Estimation  
606 of Gravity Wave Momentum Flux and Phase Speeds from Quasi-Lagrangian Strato-  
607 spheric Balloon Flights. Part II: Results from the Vorcore Campaign in Antarctica. *J.*  
608 *Atmos. Sci.*, *65*(10), 3056–3070. doi: 10.1175/2008JAS2710.1
- 609 Hertzog, A., Cocquerez, P., Guilbon, R., Valdivia, J.-N., Venel, S., Basdevant, C., ...  
610 E.Schmitt (2007). Stratéole/Vorcore—Long-duration, Superpressure Balloons to  
611 Study the Antarctic Lower Stratosphere during the 2005 Winter. *J. Atmos. Oceanic*  
612 *Technol.*, *24*, 2048–2061. doi: 10.1175/2007JTECHA948.1
- 613 Hertzog, A., & Vial, F. (2001). A study of the dynamics of the equatorial lower stratosphere  
614 by use of ultra-long-duration balloons: 2. Gravity waves. *J. Geophys. Res.*, *106*, 22745–  
615 22761. doi: 10.1029/2000JD000242
- 616 Holt, L. A., Lott, F., Garcia, R. R., Kiladis, G. N., Cheng, Y., Anstey, J. A., ... Yukimoto,  
617 S. (2020). An evaluation of tropical waves and wave forcing of the QBO in the  
618 QBOi models. *Quarterly Journal of the Royal Meteorological Society*, qj.3827. doi:  
619 10.1002/qj.3827
- 620 Holton, J. R., Haynes, P. H., McIntyre, M. E., Douglass, A. R., Rood, R. B., & Pfister,  
621 L. (1995). Stratosphere-troposphere exchange. *Rev. Geophys.*, *33*, 403–439. doi:

- 622 10.1029/95RG02097
- 623 Janowiak, J., Joyce, B., & Xie, P. (2017). *NCEP/CPC L3 Half Hourly 4km Global (60S -*  
624 *60N) Merged IR V1*. Edited by Andrey Savtchenko, Greenbelt, MD, Goddard Earth  
625 Sciences Data and Information Services Center (GES DISC). (Accessed 2020)
- 626 Jensen, E. J., Pfister, L., Bui, T.-P., Lawson, P., & Baumgardner, D. (2010). Ice nucleation  
627 and cloud microphysical properties in tropical tropopause layer cirrus. *Atmos. Chem.*  
628 *Phys.*, *10*, 1369–1384. doi: 10.5194/acp-10-1369-2010
- 629 Jensen, E. J., Pfister, L., Jordan, D. E., Fahey, D. W., Newman, P. A., Thornberry, T., ...  
630 others (2013). The NASA Airborne Tropical Tropopause Experiment (ATTREX).  
631 *SPARC Newsletter*, *41*, 15–24.
- 632 Jensen, E. J., Ueyama, R., Pfister, L., Bui, T. V., Alexander, M. J., Podglajen, A., ...  
633 Schoeberl, M. R. (2016). High-frequency gravity waves and homogeneous ice nucle-  
634 ation in tropical tropopause layer cirrus. *Geophys. Res. Lett.*, *43*, 6629–6635. doi:  
635 10.1002/2016GL069426
- 636 Jewtoukoff, V., Plougonven, R., & A.Hertzog. (2013). Gravity waves generated by deep  
637 tropical convection: Estimates from balloon observations and mesoscale simulations.  
638 *J. Geophys. Res.*, *118*, 9690–9707. doi: <https://doi.org/10.1002/jgrd.50781>
- 639 Karoly, D. J., Roff, G. L., & Reeder, M. J. (1996). Gravity wave activity associated with  
640 tropical convection detected in TOGA COARE Sounding data. *Geophys. Res. Lett.*,  
641 *23*, 261–264. doi: 10.1029/96gl00023
- 642 Kawatani, Y., Watanabe, S., Sato, K., Dunkerton, T. J., Miyahara, S., & Takahashi, M.  
643 (2010). The Roles of Equatorial Trapped Waves and Internal Inertia–Gravity Waves in  
644 Driving the Quasi-Biennial Oscillation. Part I: Zonal Mean Wave Forcing. *J. Atmos.*  
645 *Sci.*, *67*, 963–980. doi: 10.1175/2009JAS3222.1
- 646 Kim, J.-E., & Alexander, M. J. (2015). Direct impacts of waves on tropical cold point  
647 tropopause temperature. *Geophys. Res. Lett.*, *42*, 1584–1592. doi: [https://doi.org/](https://doi.org/10.1002/2014GL062737)  
648 [10.1002/2014GL062737](https://doi.org/10.1002/2014GL062737)
- 649 Lane, T. P., & Moncrieff, M. W. (2008). Stratospheric gravity waves generated by multiscale  
650 tropical convection. *J. Atmos. Sci.*, *65*, 2598–2614. doi: 10.1175/2007JAS2601.1
- 651 Lane, T. P., Reeder, M. J., & Clark, T. L. (2001). Numerical Modeling of Gravity Wave  
652 Generation by Deep Tropical Convection. *J. Atmos. Sci.*, *58*, 1249–1274. doi: 10.1175/  
653 1520-0469(2001)058<1249:NMOGWG>2.0.CO;2
- 654 Lane, T. P., & Sharman, R. D. (2006). Gravity wave breaking, secondary wave generation,  
655 and mixing above deep convection in a three-dimensional cloud model. *Geophys. Res.*  
656 *Lett.*, *33*. doi: 10.1029/2006GL027988
- 657 Lane, T. P., & Zhang, F. (2011). Coupling between Gravity Waves and Tropical Convection  
658 at Mesoscales. *J. Atmos. Sci.*, *68*, 2582–2598. doi: 10.1175/2011JAS3577.1
- 659 Larsen, M. F., Swartz, W. E., & Woodman, R. F. (1982). Gravity-wave generation by  
660 thunderstorms observed with a vertically-pointing 430 MHz radar. *Geophys. Res.*  
661 *Lett.*, *9*, 571–574. doi: 10.1029/GL009i005p00571
- 662 Liu, C., & Zipser, E. J. (2005). Global distribution of convection penetrating the tropical  
663 tropopause. *J. Geophys. Res.*, *110*. doi: 10.1029/2005JD006063
- 664 Lu, B., & Ren, H.-L. (2020). What Caused the Extreme Indian Ocean Dipole Event in  
665 2019? *Geophys. Res. Lett.*, *47*(11). doi: 10.1029/2020gl087768
- 666 Madden, R. A., & Julian, P. R. (1971). Detection of a 40–50 Day Oscillation in the  
667 Zonal Wind in the Tropical Pacific. *J. Atmos. Sci.*, *28*, 702–708. doi: 10.1175/  
668 1520-0469(1971)028<0702:DOADOI>2.0.CO;2
- 669 Madden, R. A., & Julian, P. R. (1972). Description of Global-Scale Circulation Cells in  
670 the Tropics with a 40–50 Day Period. *J. Atmos. Sci.*, *29*, 1109–1123. doi: 10.1175/  
671 1520-0469(1972)029<1109:DOGSCC>2.0.CO;2
- 672 Matsuno, T. (1966). Quasi-geostrophic motions in the equatorial area. *J. Meteorol. Soc. of*  
673 *Japan. Ser. II*, *44*, 25–43. doi: 10.2151/jmsj1965.44.1.25
- 674 Pahlavan, H. A., Wallace, J. M., Fu, Q., & Kiladis, G. N. (2021). Revisiting the Quasi-  
675 Biennial Oscillation as Seen in ERA5. Part II: Evaluation of Waves and Wave Forcing.  
676 *J. Atmos. Sci.*, *78*, 693–707. doi: 10.1175/jas-d-20-0249.1

- 677 Pfister, L., Scott, S., Loewenstein, M., Bowen, S., & Legg, M. (1993). Mesoscale Dis-  
678 turbances in the Tropical Stratosphere Excited by Convection: Observations and Ef-  
679 fects on the Stratospheric Momentum Budget. *J. Atmos. Sci.*, *50*, 1058–1075. doi:  
680 10.1175/1520-0469(1993)050<1058:MDITTS>2.0.CO;2
- 681 Piani, C., Durran, D., Alexander, M. J., & Holton, J. R. (2000). A numerical study  
682 of three-dimensional gravity waves triggered by deep tropical convection and their  
683 role in the dynamics of the QBO. *J. Atmos. Sci.*, *57*, 3689–3702. doi: 10.1175/  
684 1520-0469(2000)057<3689:ANSOTD>2.0.CO;2
- 685 Plougonven, R., Hertzog, A., & Guez, L. (2013). Gravity waves over Antarctica and the  
686 Southern Ocean: consistent momentum fluxes in mesoscale simulations and strato-  
687 spheric balloon observations. *Quarterly Journal of the Royal Meteorological Society*,  
688 *139*, 101–118. doi: 10.1002/qj.1965
- 689 Podglajen, A., Hertzog, A., Plougonven, R., & Legras, B. (2016). Lagrangian tempera-  
690 ture and vertical velocity fluctuations due to gravity waves in the lower stratosphere.  
691 *Geophys. Res. Lett.*, *43*, 3543–3553. doi: 10.1002/2016GL068148
- 692 Podglajen, A., Hertzog, A., Plougonven, R., & Legras, B. (2020). Lagrangian gravity wave  
693 spectra in the lower stratosphere of current (re)analyses. *Atmos. Chem. Phys.*, *20*,  
694 9331–9350. doi: 10.5194/acp-20-9331-2020
- 695 Podglajen, A., Hertzog, A., Plougonven, R., & Žagar, N. (2014). Assessment of the accuracy  
696 of (re)analyses in the equatorial lower stratosphere. *J. Geophys. Res.*, *119*, 166–188.  
697 doi: <https://doi.org/10.1002/2014JD021849>
- 698 Podglajen, A., Plougonven, R., Hertzog, A., & Jensen, E. (2018). Impact of gravity waves  
699 on the motion and distribution of atmospheric ice particles. *Atmos. Chem. Phys.*,  
700 10799–10823. doi: 10.5194/acp-18-10799-2018
- 701 Preusse, P., Eckermann, S. D., & Ern, M. (2008). Transparency of the atmosphere to short  
702 horizontal wavelength gravity waves. *J. Geophys. Res.*, *113*, D24104. doi: 10.1029/  
703 2007JD009682
- 704 Randel, W. J., Wu, F., & Podglajen, A. (2021). Equatorial Waves, Diurnal Tides and  
705 Small-Scale Thermal Variability in the Tropical Lower Stratosphere From COSMIC-2  
706 Radio Occultation. *J. Geophys. Res.*, *126*. doi: 10.1029/2020jd033969
- 707 Richter, J. H., Butchart, N., Kawatani, Y., Bushell, A. C., Holt, L., Serva, F., . . . Yukimoto,  
708 S. (2020). Response of the Quasi-Biennial Oscillation to a warming climate in global  
709 climate models. *Qu. J. Roy. Meteor. Soc.*, 1 – 29. doi: <https://doi.org/10.1002/qj.3749>
- 710 Saji, N. H., Goswami, B. N., Vinayachandran, P. N., & Yamagata, T. (1999). A dipole  
711 mode in the tropical Indian Ocean. *Nature*, *401*, 360–363. doi: 10.1038/43854
- 712 Schirber, S., Manzini, E., Krismer, T., & Giorgetta, M. (2015). The quasi-biennial oscillation  
713 in a warmer climate: sensitivity to different gravity wave parameterizations. *Climate*  
714 *Dyn.*, *45*, 825–836. doi: 10.1007/s00382-014-2314-2
- 715 Solomon, S., Rosenlof, K. H., Portmann, R. W., Daniel, J. S., Davis, S. M., Sanford,  
716 T. J., & Plattner, G.-K. (2010). Contributions of Stratospheric Water Vapor to  
717 Decadal Changes in the Rate of Global Warming. *Science*, *327*, 1219–1223. doi:  
718 10.1126/science.1182488
- 719 Stephan, C., & Alexander, M. J. (2015, jun). Realistic simulations of atmospheric gravity  
720 waves over the continental U.S. using precipitation radar data. *J. Adv. Mod. Earth*  
721 *Syst.*, *7*(2), 823–835. doi: 10.1002/2014ms000396
- 722 Torrence, C., & Compo, G. P. (1998). A Practical Guide to Wavelet Analysis. *Bull. Am.*  
723 *Meteorol. Soc.*, *79*, 61–78. doi: 10.1175/1520-0477(1998)079<0061:APGTWA>2.0.CO;  
724 2
- 725 Vial, F., Hertzog, A., Mechoso, C. R., Basdevant, C., Cocquerez, P., Dubourg, V., &  
726 F.Nouel. (2001). A study of the dynamics of the equatorial lower stratosphere by use of  
727 ultra-long-duration balloons: 1. Planetary scales. *J. Geophys. Res.*, *106*, 22725–22743.  
728 doi: 10.1029/2000JD000241
- 729 Vincent, R. A., & Alexander, M. J. (2020). Observational studies of short vertical wavelength  
730 gravity waves and interaction with QBO winds. *J. Geophys. Res.*, *27*. doi: 10.1029/  
731 2020JD032779

- 732 Vincent, R. A., & Hertzog, A. (2014). The response of superpressure balloons to gravity  
733 wave motions. *Atmos. Meas. Tech.*, *7*, 1043–1055. doi: 10.5194/amt-7-1043-2014
- 734 Vincent, R. A., Hertzog, A., Boccara, G., & Vial, F. (2007). Quasi-Lagrangian super-  
735 pressure balloon measurements of gravity-wave momentum fluxes in the polar strato-  
736 sphere of both hemispheres. *Geophys. Res. Lett.*, *34*. doi: [https://doi.org/10.1029/  
737 2007GL031072](https://doi.org/10.1029/2007GL031072)
- 738 Webster, P. J., Moore, A. M., Loschnigg, J. P., & Leben, R. R. (1999). Coupled  
739 ocean–atmosphere dynamics in the indian ocean during 1997–98. *Nature*, *401*, 356–  
740 360. doi: 10.1038/43848
- 741 Wright, C. J., Osprey, S. M., & Gille, J. C. (2013). Global observations of gravity wave  
742 intermittency and its impact on the observed momentum flux morphology. *J. Geophys.*  
743 *Res.*, *118*, 10,980–10,993. doi: 10.1002/jgrd.50869
- 744 Zhang, G. J., & Mu, M. (2005). Simulation of the Madden–Julian Oscillation in the NCAR  
745 CCM3 Using a Revised Zhang–McFarlane Convection Parameterization Scheme. *J.*  
746 *Climate*, *18*, 4046–4064. doi: 10.1175/JCLI3508.1